RSC Advances

PAPER

View Article Online
View Journal | View Issue

Cite this: *RSC Adv.*, 2023, **13**, 3112

Synthesis and properties of SiO_2/SiO_2@Ag two-phase STFs†

Caiting He,[ab] Qiushi Wang,[*ab] Xiaoya Jia,[ab] Jie Liu,[ab] Runjun Sun[ab] and Meiyu Chen[*ab]

Soft body armor with a strain-sensing function using conductive shear thickening fluids (STFs) has gradually gained research interest. In this study, conductive SiO_2@Ag core–shell microspheres were synthesized and the influence of process parameters on their properties was evaluated. Subsequently, SiO_2 and SiO_2@Ag were used as dispersed phases to prepare two-phase STFs, the effect of the core–shell microspheres' proportion on the rheological properties of the STFs was investigated, and its mechanism was discussed. The results indicated that SiO_2@Ag core–shell microspheres were coated with elemental silver and when the concentration of sodium hydroxide and glucose were 0.07 and 0.09 mol L^{-1}, respectively, the coating surface was the most uniform and compact, and the conductivity reached the minimum value of 0.56 Ω cm. The two-phase STFs exhibited good and reversible shear thickening behaviors and the critical shear rate decreased with increasing core–shell microsphere concentration. Additionally, when the mass fraction of SiO_2 and SiO_2@Ag core–shell microspheres was 45% and 20%, respectively, the thickening rate was 325%, and the resistance of two-phase STFs decreased simultaneously with the emergence of shear thickening that reached the lowest value of 795.16 kΩ. This study provides a novel strategy for synthesizing conductive STFs for strain-sensing flexible stab-resistant composites.

Received 31st October 2022
Accepted 16th January 2023

DOI: 10.1039/d2ra06895h

rsc.li/rsc-advances

1 Introduction

Shear Thickening Fluids (STFs) are non-Newtonian fluids whose physical state rapidly changes from liquid to solid state when subjected to shear action exceeding the critical rate,[1–3] and this phase transition is reversible and reproducible.[4,5] STFs are extensively used in dampers,[6] hydraulic couplers,[7] shock absorption,[8] and other engineering fields. In the 1990s, Professor Wagner from Delaware State University and Dr Wetzel from the US Army Research Laboratory successfully expanded the application of STFs to the field of personal protection.[9,10]

The rheological properties of STFs served as the foundation for their use in personal protection applications. The concentration, type, and size of the dispersed phase influence the microstructure and rheological properties of the STFs.[11,12] Grover *et al.*[11] concluded that the optimal process conditions whereby STFs reduced the impact velocity of the projectile were achieved at a concentration of 67% and particle size of 600 nm, and the increased friction and volume occupation between the SiO_2 particles with larger sizes was proposed to be the main reason for the enhancement in the STFs energy absorption. Gurgen *et al.*[3,13] and Hasanzadeh *et al.*[14,15] investigated the influence of the addition of silicon carbide (SiC) and multi-walled carbon nanotubes (MWCNT) as the dispersed phase on the rheological properties of the two-phase STFs, which weakened the shear thickening effect by the degradation of the suspensions' network structure. Li *et al.*[16] used oxygen plasma treatment to graft hydroxyl, carboxyl, and other oxygen functional groups onto the MWCNT surface, and the formation of hydrogen bonds between the oxygen functional groups and particles in the STFs was reported to be the main reason for the improved shear thickening effect.

In addition to meeting the basic rheological property requirements, multi-phase STFs can be synthesized by introducing conductive carbon-based additions to provide intelligent functions such as strain or force sensing.[17,18] Chen *et al.*[7] prepared conductive STFs using carbon nanotubes (CNTs). The mass fraction of SiO_2 and CNTs affected the resistance of C-STFs, which was negatively correlated with STFs thickening. Zhang *et al.*[19] prepared a C-STF/Ecoflex material for sensors by adding CNTs to STFs, and developed a flexible composite for multifunction applications. Wang and Liu *et al.*[20,21] obtained a flexible material with a high sensing sensitivity and excellent protective performance by combining conductive STFs with CNTs and Kevlar fabric, which monitored the different motion states of the human body. Zhou[22] *et al.* used shear-toughened gel (SSG), two-dimensional MXene, and Kevlar to prepare the MXene/SSG/Kevlar composites with good electrical conductivity

[a]*School of Textile Science and Engineering, Xi'an Polytechnic University, Xi'an, Shaanxi 710048, China. E-mail: yuanshijidi@163.com; wangqiushi@xpu.edu.cn*
[b]*Key Laboratory of Functional Textile Material and Product (Xi'an Polytechnic University), Ministry of Education, Xi'an, Shaanxi 710048, China*

† Electronic supplementary information (ESI) available. See DOI: https://doi.org/10.1039/d2ra06895h

impact resistance. Zhang *et al.*[23] prepared impregnated conductive Shear Thickening Gel (STG) by adding carbon black (CB) into a polyurethane sponge (PUS). The developed STG-CB-PUS composite material effectively tracked human movements, such as walking, running, and jumping. Zhao *et al.*[24] developed a CB-STG/Kevlar composite that exhibited good mechanical-electrical coupling characteristics, and the resistance of the material was linearly related to the impact force. Fan[25] *et al.* used reduced graphene oxide (RGO) and nano-silica/shear-thickened gel to manufacture the SiO_2/STG/RGO@Kevlar composites as a protective layer with good impact resistance, and strain sensing.

From above, carbon-based materials, such as CNTs and CB, were generally selected to add into STFs to prepare conductive STFs, further endowing STFs-based flexible composites with sensing functions. However, no research has been reported on the preparation of conductive STFs using metal materials with lower resistivities, such as Ag and Cu. Therefore, we synthesize SiO_2@Ag core–shell microspheres by planting Ag nanoparticles on the SiO_2 microsphere surface, aiming to design the STFs with both shear thickening and strain-sensing characteristics.

2 Experimental section

2.1 Materials

Monodispersed silica microspheres (SiO_2) with a particle size of 500 nm were purchased from Shanghai Bowei Applied Materials Technology Co. Ltd. Glucose ($C_6H_{12}O_6$), sodium hydroxide (NaOH), silver nitrate ($AgNO_3$), ammonia (NH_4OH), anhydrous ethanol, (3-mercaptopropyl) trimethoxysilane (MPTMS), and polyethylene glycol 200 (PEG200) were all of the analytical grade and purchased from Sinopharm Group Chemical Reagent Co. Deionized water was used for all the experiments.

2.2 Synthesis of SiO_2@Ag core–shell microspheres

A certain mass of SiO_2 modified by surface sulfhydrylation (see the ESI† for the detailed method) was added into a reducing solution containing a specific concentration of aqueous $C_6H_{12}O_6$ and NaOH, and ultrasonically dispersed for 10–15 min. Ammonia was added dropwise to a certain mass of the plating solution (0.12 mol L^{-1} $AgNO_3$ aqueous solution) until the turbidity of the mixture was clarified. Subsequently, the resultant mixture was added dropwise to the reducing solution under 300 rad min^{-1} magnetic stirring at 1 mL min^{-1}, and the reaction was complete after 40 min. After the reaction was completed, the resulting mixture was centrifuged, washed with anhydrous ethanol for 3–5 times, and then dried at 60 °C in a vacuum oven without additional protective atmosphere to obtain SiO_2@Ag core–shell microspheres. The flow chat is shown in Fig. 1a.

Based on the preliminary experimental results, the appropriate concentration ranges of NaOH and $C_6H_{12}O_6$ were 0.03–0.07 mol L^{-1} and 0.09–0.13 mol L^{-1}, respectively. The specific experimental protocols are listed in Table S1 in the ESI.†

2.3 Synthesis of STFs

STFs were synthesized using the ultrasonic dispersion method. First, a certain amount of SiO_2 was weighed and dried at 60 °C. Subsequently, it was added to a beaker containing an appropriate amount of anhydrous ethanol, and ultrasonically dispersed for 30 min. A certain amount of PEG200 was added under continuous ultrasonic dispersion, followed by a certain amount of SiO_2@Ag core–shell microspheres, and the mixture was continuously sonicated until a uniform STF suspension formed. Finally, the residual anhydrous ethanol and air bubbles were removed by vacuum drying at 60 °C for 24 h, and the resulting suspension was sealed and stored for later use. A photo of the prepared two-phase STFs is shown in Fig. S1 in the ESI.† The flow chat is shown in Fig. 1b. The specific experimental protocols for synthesizing the two-phase STFs are listed in Table S2 in the ESI.†

2.4 Testing and characterization

2.4.1 Field-emission scanning electron microscopy (FESEM) and X-ray energy dispersive spectroscopy (EDS). The morphology and coating effect of SiO_2 and SiO_2@Ag core–shell microspheres were characterized by field-emission scanning electron microscopy (FESEM; QUANTA 450-FEG, FEI, USA). The contents of Ag, Si, and other elements in the samples and Ag distribution on the SiO_2@Ag core–shell microsphere surface were analyzed by X-ray energy dispersive spectroscopy (EDS).

2.4.2 Transmission electron microscope (TEM). The thickness of SiO_2@Ag core–shell microspheres was characterized by transmission electron microscopy (H-7650B, Hitachi, Japan) operating at 80 kV.

2.4.3 X-ray powder diffraction (XRD). SiO_2 and SiO_2@Ag powders were characterized by X-ray diffraction (XRD; DMAX-RAPID II, Rigaku, Japan). Test conditions: tube current = 200 mA, tube voltage = 40 kV, scanning range = 5–80°, scanning speed = 8° per min.

2.4.4 Resistivity test of SiO_2@Ag core–shell microsphere assemblies. SiO_2@Ag core–shell microsphere powder (0.3 g) was added into a straight-mouth syringe (3 mL), and a copper piece connected to a wire was placed near the syringe needle tip, and another copper piece attached to a wire was placed on the side of the syringe plunger. Subsequently, the powder was compacted to a thickness of 4 mm. A low resistance meter (Milli-Ohmmeter MO-3, Fischer, Germany) was used to test and calculate the resistivity of the powder. The resistance test time was 60 s, and each sample was tested 5 times to obtain an average value to ensure the accuracy of the experimental results. A schematic of the resistivity test method of the core–shell microsphere powder is shown in Fig. 2.

2.4.5 Rheological performance test. The steady-state and dynamic rheological properties of STFs samples were characterized using a rotational rheometer (MCR 302, Anton Paar, Austria). The CP25-2 rotor model was selected for the test. The diameter of the rotor was 24.97 mm, the cone Angle θ_c was 1.994°, the cone-plate distance was 0.103 mm, and the test temperature was 25 °C. All rheological tests required sample pre-shearing at 10 s^{-1} to eliminate the shear history. The shear

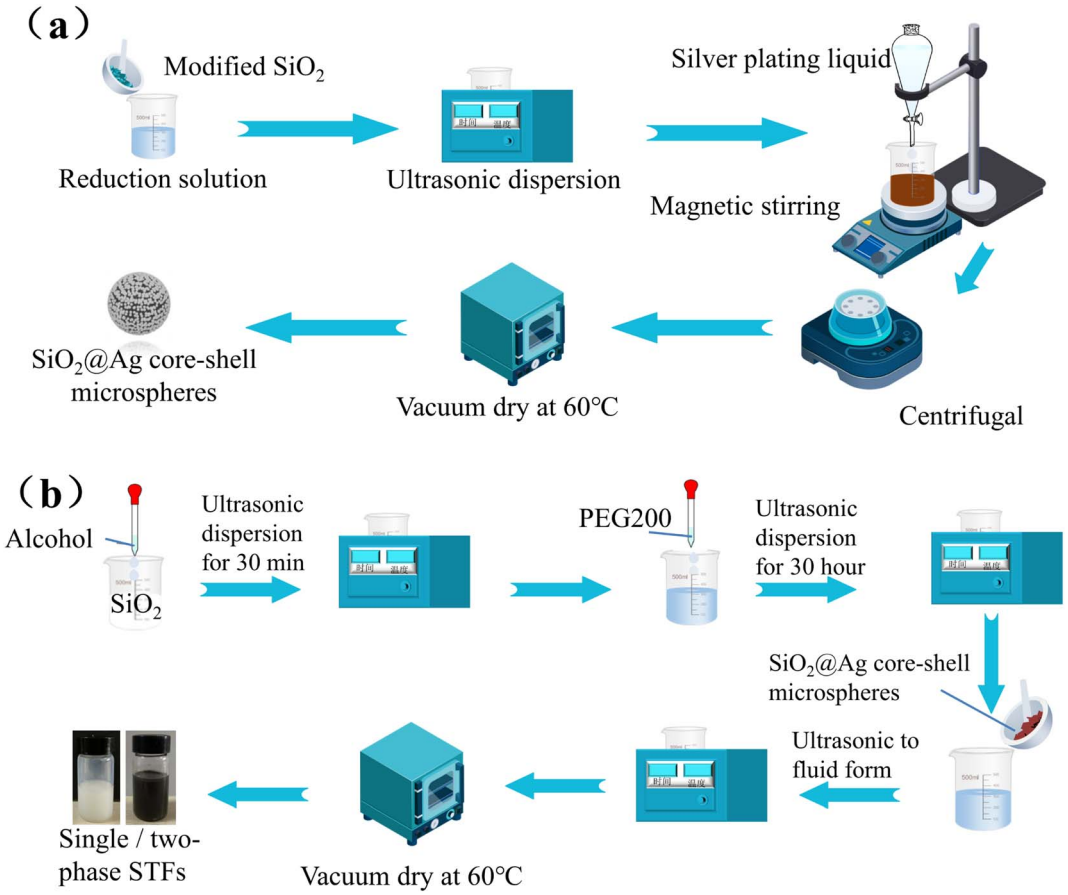

Fig. 1 Flow chart of (a) SiO_2@Ag core–shell microsphere synthesis, (b) SiO_2/SiO_2@Ag two-phase STFs preparation.

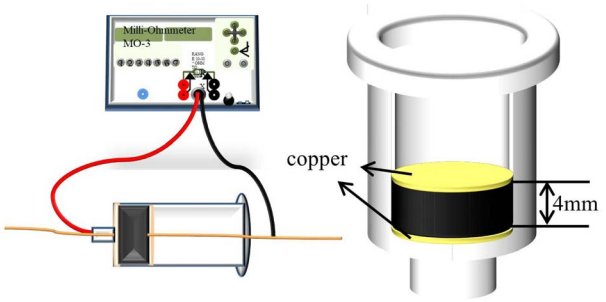

Fig. 2 Schematic of the resistivity measurement method for SiO_2@Ag core–shell microspheres.

rate test range for steady-state rheological properties was 0.01–5000 s^{-1}, the fixed angular frequency for dynamic rheological property testing was 10 rad s^{-1}, and the shear strain range was 0.01–1000%.

2.4.6 Steady-state rheological and resistance performance testing. Steady-state rheological and resistance tests were performed on the conductive STFs samples using a rotational rheometer (MCR 302, Olly Anton Paar) and source measure units (Keithley 2450, Tektronix, USA). The rheological and resistance tests were synchronized based on the test time. The CC17 rotor model was used in the test, the distance between the bottom of the barrel and the rotor was 0.3 mm, and the shear rate test range of the steady-state rheological property was 0.01–1000 s^{-1}, and the test temperature was 25 °C. The two-line method tests using the source measure units and the connection mode are shown in Fig. 3.

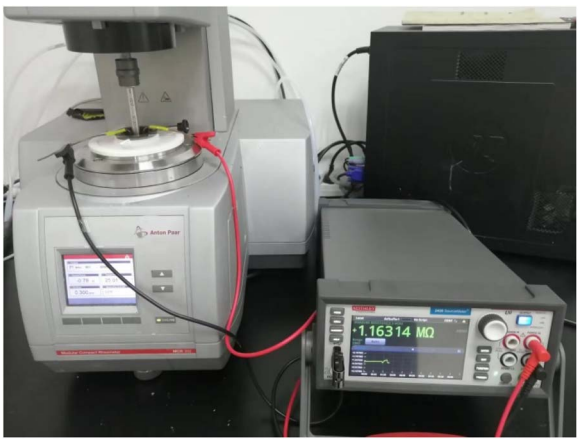

Fig. 3 Viscosity-resistance test chart of the STFs system.

3 Results and discussion

3.1 Determination of process parameters for SiO_2@Ag core–shell microsphere synthesis

3.1.1 Effect of process parameters on the morphology of SiO_2@Ag core–shell microspheres. During the electroless plating, the alkaline environment and concentration of the reducing agent are the main factors controlling the reaction rate.[26,27] Therefore, the effect of process parameters on the morphology of the SiO_2@Ag core–shell microspheres was investigated by varying the NaOH and $C_6H_{12}O_6$ concentrations in this study. The effect of the alkaline environment on the surface coating morphology of the N_xC_9 series of samples was investigated by varying the NaOH concentration at a fixed $C_6H_{12}O_6$ reducing agent concentration of 0.09 mol L^{-1}, and Fig. 4 shows the SEM images of the synthesized SiO_2@Ag core–shell microspheres and the illustration is the secondary magnification of the typical microspheres. Although the coating morphology of the N_3C_9 sample was relatively uniform and exhibited no agglomeration, the silver particles on the coating were sparse. In this case, limited OH^- ions are present in the solution, and as the reaction progresses, OH^- ions are continuously consumed, thereby hindering the complete reduction of silver ions to elemental silver, and therefore the coating layer was not dense. When the NaOH concentration was higher than 0.11 mol L^{-1}, the coating effect of the core–shell microspheres gradually deteriorates, no uniform and thick coating was observed, and the silver particles agglomerated, mainly because the NaOH concentration was too high. Excess OH^- ions increase the reaction rate, and the rapidly reduced silver particles cannot adhere to the SiO_2 surface. Therefore, when the $C_6H_{12}O_6$ reducing agent concentration was 0.09 mol L^{-1}, a NaOH concentration of 0.07 mol L^{-1} provided the most suitable alkaline environment.

For the N_7C_y series of samples, the reducing agent concentration also affects the surface coating morphology. As shown in Fig. 4, for samples N_7C_3 and N_7C_5, owing to the low concentration of the reducing agent, silver ions in solution are reduced to silver at a slow rate, which limits the number of particles adhered to the SiO_2 surface, and thereby the coating layer is thin. When the $C_6H_{12}O_6$ concentration was higher than 0.09 mol L^{-1}, the silver particles agglomerated into large particles that adhered to the SiO_2 surface, which formed a non-dense coating. In particular, for the N_7C_{13} sample, the $C_6H_{12}O_6$ concentration was too high, resulting in a highly reducible solution. In this case, the reaction rate is too rapid, and the rate of silver ion reduction is greater than the rate of Ag particle adhesion to the SiO_2 surface, and therefore the Ag particles in solutions easily formed agglomerates.

Based on the above SEM results, sample N_7C_9 exhibited the best coating effect, and the silver particles of the coating layer were relatively dense and uniform. In this case, the reaction rate was relatively moderate, the silver ion reduction rate and Ag particle adhesion to the SiO_2 surface were balanced, and the reduced silver preferentially nucleated on the SiO_2 surface, forming a continuous and dense coating layer. The TEM photograph of the N_7C_9 specimen clearly shows the SiO_2 core and silver-plating shell of the microspheres, and the thickness of the shell is about 13 nm in Fig. 5.

The content and distribution of Ag on the surface of the N_7C_9 sample were further analyzed. The proportion of the main elemental content on the sample surface and the mapping sweep distribution of elemental Ag determined by EDS are shown in Fig. 6. The magnification of the EDS mapping sweep image is 100 000 times which are twice that of the SEM photo of N_7C_9 sample. Based on the distribution of green spots, elemental Ag was uniformly distributed on the surface of the SiO_2 microspheres. Additionally, the main elements on the surface of the SiO_2@Ag core–shell microspheres were O, Si, and Ag, and the proportion of elemental Ag was 0.76%.

3.1.2 Phase analysis of SiO_2@Ag core–shell microspheres. As shown in Fig. 7a and b, the crystal structure of the N_xC_y series samples were analyzed by XRD. All this pattern depicts a similar crystal structure, *i.e.*, the presence of distinct crystalline peaks at 38.12°, 44.30°, 64.44°, and 77.40°, and a insignificant prominent broad near 22°.The phase composition and crystal structure of the pure SiO_2 and SiO_2@Ag core–shell microsphere N_7C_9 samples were compared in Fig. 7c, which confirmed the presence of elemental silver in the SiO_2@Ag core–shell microsphere sample. Pure SiO_2 exhibited a prominent broad peak at 22°, indicating that it is amorphous. In addition to the central broad peak of SiO_2, the SiO_2@Ag core–shell microsphere sample also exhibited four characteristic diffraction peaks at 2θ values of 38.12°, 44.30°, 64.44°, and 77.40°, which correspond to different crystal planes of face-centered cubic Ag, namely (111), (200), (220), and (311),[26] respectively. This is basically the same as the Ag phase jcpds card number PDF#65-2871 standard card. Notably, no diffraction peaks of other silver compounds were detected. Because of the difference in resistivity between elemental silver and silver compounds, XRD analysis confirmed the surface of the SiO_2@Ag core–shell microspheres was coated with elemental silver, which provides a foundation for the subsequent preparation of STFs with reduced resistivity.

As shown in Fig. 7d, the grain size of the silver plating layer of N_xC_y series specimens was calculated by Scherrer equation. And the N_7C_9 specimen has the smallest average grain size of 3.42 nm, which is consistent with the morphology of microspheres in Fig. 4.

3.1.3 Effect of process parameters on the electrical properties of SiO_2@Ag core–shell microsphere aggregates. The resistivity of the SiO_2@Ag core–shell microspheres is an essential factor that influences the electrical conductivity and strain-sensing function of SiO_2@Ag/PEG200-based STFs. By evaluating the influence of process parameters on the resistivity of the SiO_2@Ag core–shell microsphere aggregates, the optimal process for synthesizing core–shell microspheres was further determined. Fig. 8a and b show the resistivity test results of the N_xC_9 and N_7C_y series of samples, respectively. The resistivity of the N_7C_y series was lower than that of the N_xC_9 series, and the variation trend in the resistivity of the SiO_2@Ag core–shell microspheres corresponds with the SEM analysis of the coating morphology. The resistivity of N_7C_9 with the most uniform and dense coating was the smallest (0.56 Ω cm). In contrast, $N_{23}C_9$,

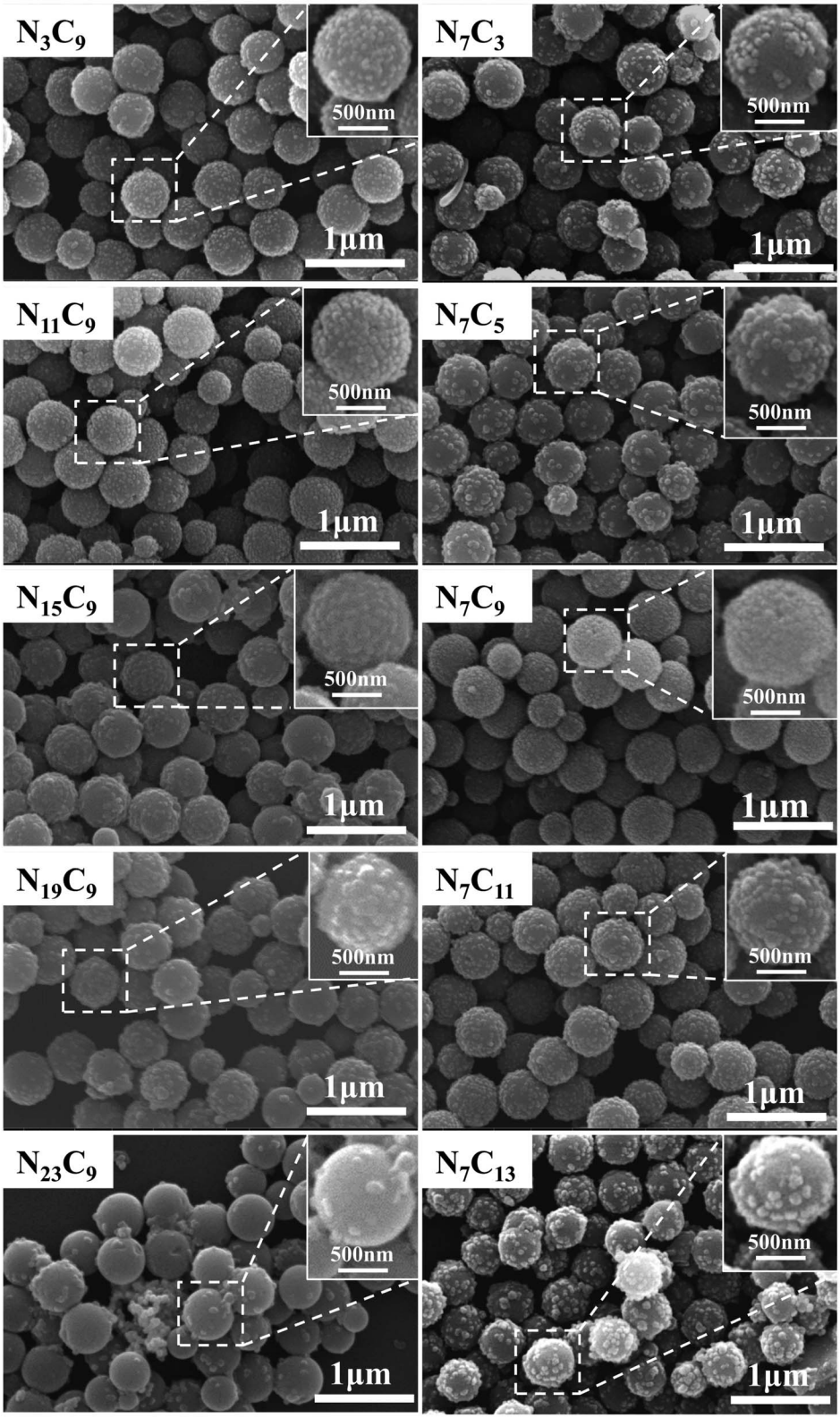

Fig. 4 SEM images and illustration (secondary magnification) of SiO_2@Ag core–shell microspheres synthesized with different process parameters.

which had the worst coating effect, exhibited the highest resistivity (1.32 Ω cm). Thus, it was concluded that the resistivity of the SiO_2@Ag core–shell microspheres is related to the uniformity and density of the SiO_2@Ag coating layer. When the

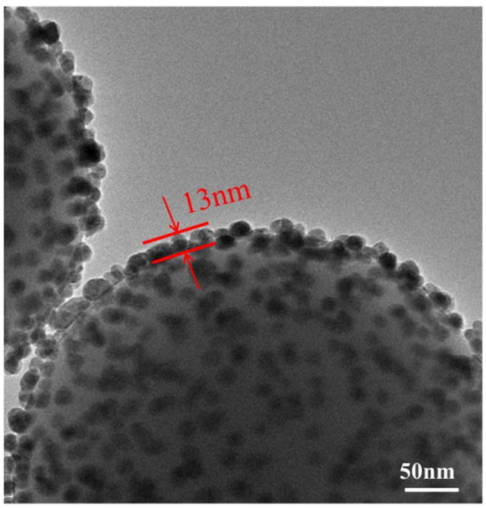

Fig. 5 TEM images of N_7C_9 core–shell microspheres.

coating is uniform and dense, the surface contact of the core–shell microspheres in the composite microsphere aggregate is good. Therefore, the resistivity was lower. Conversely, when the plating effect was poor, it was difficult for the silver layer to form a conductive pathway, and therefore the resistivity was the largest.

Based on the morphological analysis and resistivity test results, the optimal process parameters for synthesizing SiO_2@Ag core–shell microspheres are a $C_6H_{12}O_6$ concentration of 0.09 mol L^{-1} and NaOH concentration of 0.11 mol L^{-1}.

3.2 Rheological properties of the two-phase STFs system

3.2.1 Effect of the dispersed phase ratio on the rheological properties of the two-phase STFs system. The rheological properties and shear thickening mechanism of the single-phase SiO_2 system are shown in Fig. S2.† Within a specific range, increasing the concentration of the dispersed phase improved the shear thickening effect. Therefore, the effect of different ratios of the two dispersed phases on the thickening effect of the conductive STFs system was evaluated by adding SiO_2@Ag core–shell microspheres. Repeated tests using the two-phase STFs system demonstrated that when the SiO_2 mass fraction was 40% and the SiO_2@Ag mass fraction was 25%, the maximum mass fraction of each dispersed phase was achieved for the two-phase STFs system. When the mass fraction of the dispersed phase was further increased, the two-phase STFs system changed from liquid to solid state, thereby losing its fluidity in ultrasound and drying.

Fig. 9 shows the relationship between the shear rate and (a) viscosity and (b) shear stress, as well as (c) the mechanism of the two-phase STFs system. As shown in Fig. 9a, after SiO_2@Ag core–shell microsphere addition, the rheological properties of the two-phase STFs system were consistent with the variation in viscosity of the single-phase sample, which exhibited the behavior of non-Newtonian fluid. Because the density of the core–shell microspheres was larger than that of SiO_2, the density of the two-phase STFs system increased with the increase in the mass fraction of the core–shell microspheres. For STFs with a higher density, the adhesion between solid particles is stronger, and therefore the overall viscosity of the fluid increases.[3] Additionally, the decrease in the critical shear rate may be attributed to the increased viscosity of the two-phase STFs system. According to eqn (1) for calculating $F_{hydrodynamic}$,[28] viscosity is proportional to the fluid power, and thus the two-phase dispersed phase in the STF system forms hydroclusters more easily. For all the curves, the viscosity of the $STF_{60:5}$ system increased from 0.84 to 4.75 Pa s at the critical shear rate, and the thickening rate was 565%. Compared with the single-phase STFs system with 65% SiO_2 concentration, the maximum viscosity was increased by 47.37%. The viscosity of $STF_{45:20}$ increased from 2.77 to 9 Pa s at the critical shear rate, and the thickening rate was 325%. However, the viscosity of the $STF_{40:25}$ system increased from 7.25 to 17.3 Pa s at the critical shear rate, and the thickening rate was only 239%. Although the SiO_2 and SiO_2@Ag core–shell microspheres both participate in hydroclusters' formation which determines the shear thickening behavior, the weaken of shear thickening with the higher ratio of SiO_2@Ag might be due to the decrease of Si–OH on the

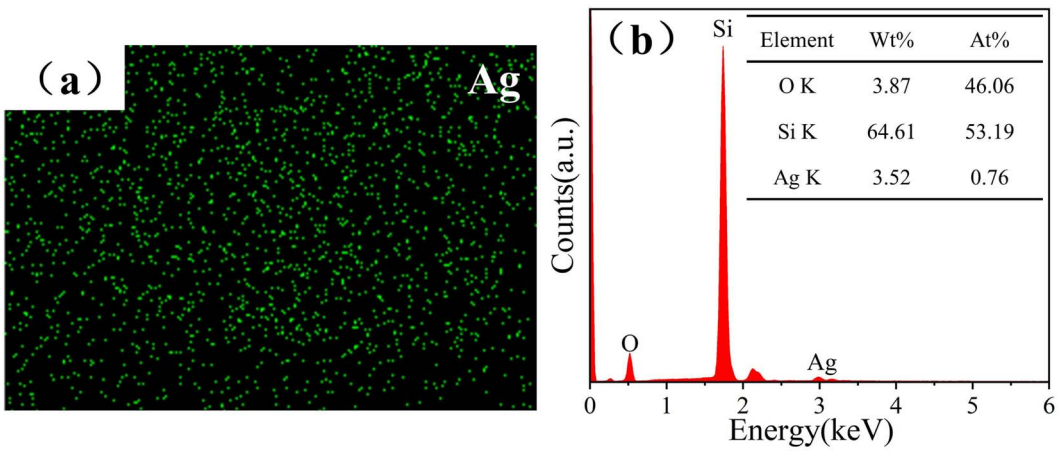

Fig. 6 (a) EDS scan and (b) EDS spectrum of N_7C_9 core–shell microspheres.

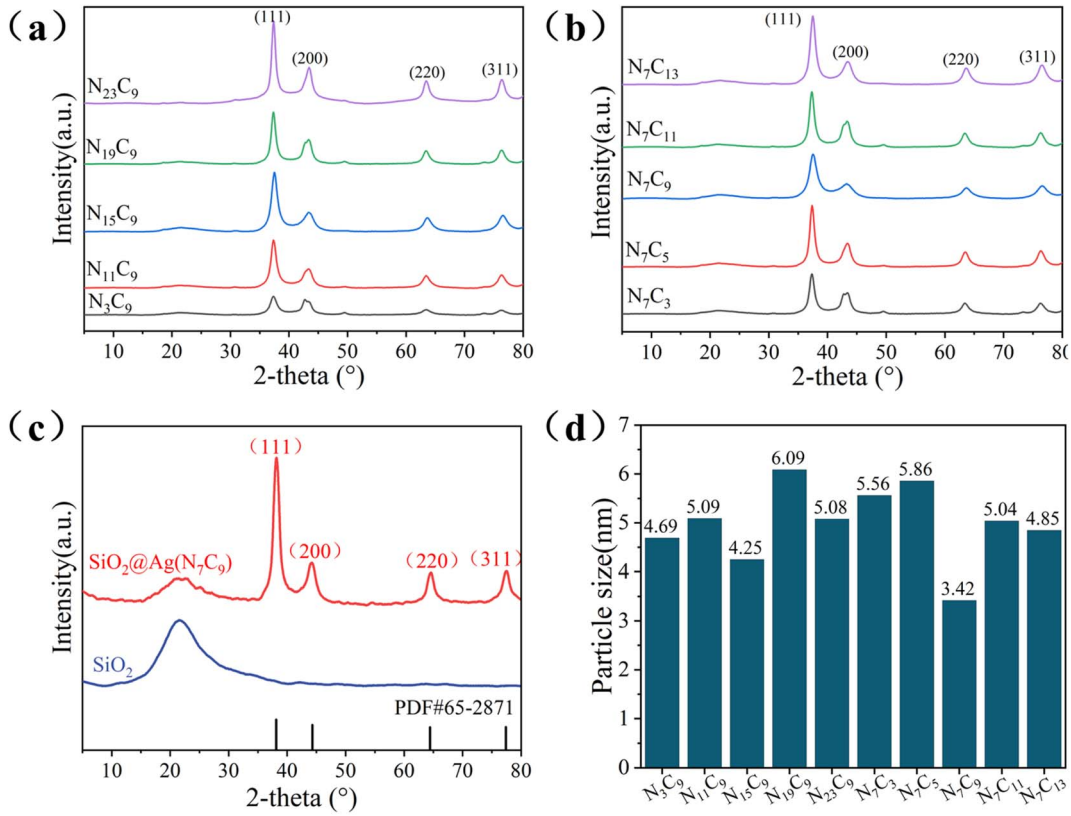

Fig. 7 XRD patterns of (a) and (b)N_xC_y series samples and (c)SiO_2 and the (d) average grain size of N_xC_y series samples.

SiO_2@Ag microspheres, leading the diminish of the hydrogen bond between Si–OH and the –OH groups in PEG200, as shown in Fig. 9(e2 and e3).

$$F_{\text{hydrodynamic}} = \frac{6\pi\eta_0\alpha^3\gamma}{h} \quad (1)$$

where η_0 is the viscosity of the dispersion medium, Pa s; α is the particle radius, mm; h is the distance between two particles, mm; γ is the shear rate, s^{-1}.

Fig. 9b shows that shear stress increased linearly with increasing shear rate during the initial stage and then increased rapidly when the critical shear rate was reached, indicating nonlinear growth. Moreover, the maximum shear stress increased with increasing mass fraction of the SiO_2@Ag core–shell microspheres. Notably, the critical shear stress of STFs with varying ratios of the dispersed phases was not different. However, the critical shear stress of the STFs system with a relatively higher SiO_2@Ag core–shell microsphere content was slightly increased.

Non-Newtonian fluids are intermediate between the solid and liquid state, and exhibit viscoelastic behavior. Based on the viscoelastic theory[24], the storage modulus (G') and loss modulus

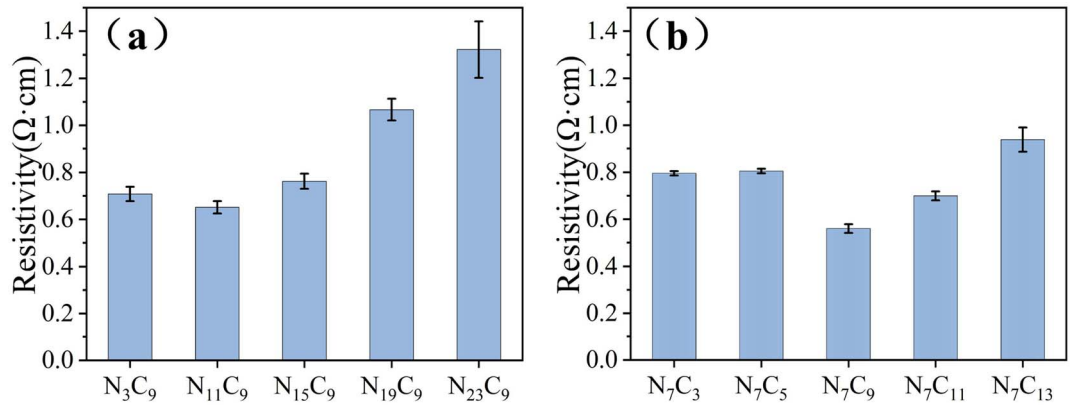

Fig. 8 Resistivity of SiO_2@Ag core–shell powders synthesized with different process parameters.

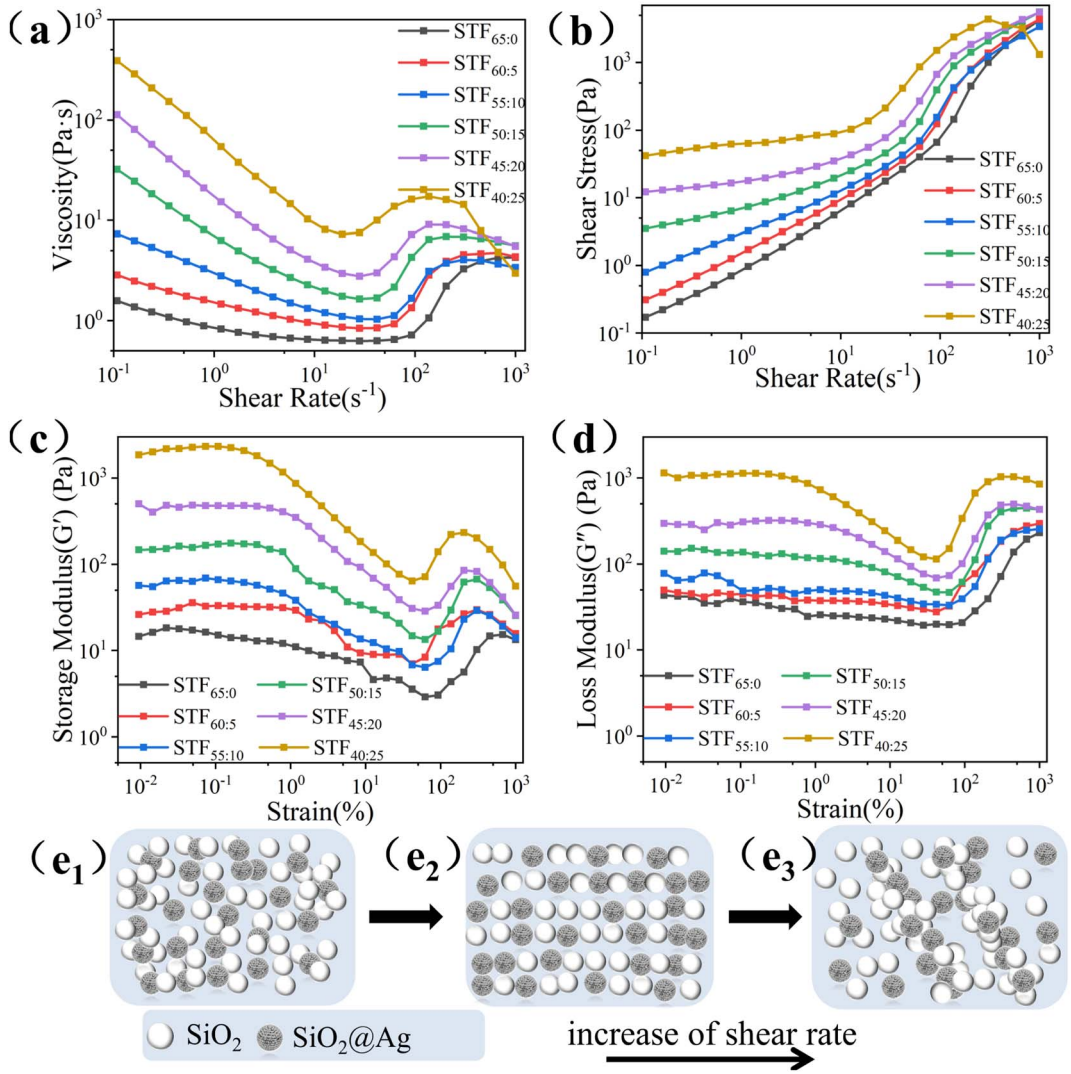

Fig. 9 Relationship between shear rate and (a) viscosity and (b) shear stress of the two-phase STFs system. Relationship between strain and the (c) energy storage modulus G' and (d) loss modulus G'' at 25 °C, and (e) the mechanism diagram.

(G'') are representative of the elastic and viscous strength of the system, respectively. The relationship between strain and the (c) energy storage modulus and (d) loss modulus of the two-phase STFs system is shown in Fig. 9. STF with different ratios of the dispersed phase exhibited the process of thinning and thickening by shear, and the overall trend was consistent. Under lower strain, G' and G'' remained unchanged because the network structure damage caused by fluid repulsion and Brownian motion was rapidly restored. Subsequently, with increasing strain, the G' and G'' curves both exhibited a downward trend. In this case, intermolecular force and Brownian motion are insufficient to restore the damaged structure. However, G'' was always greater than G', which is mainly attributed to energy dissipation and indicates the viscous nature of the system. After the critical strain was reached, the STFs system was mainly dominated by fluid force, leading to the rapid formation of hydroclusters. Both G' and G'' curves increased, and G'' was still larger than G'. In this case, G'' is dominant, indicating that the system still exhibits viscous behavior, which is consistent with the steady-state rheological behavior of the system, which exhibited a relatively low thickening rate.

3.2.2 Reversible performance analysis of the two-phase STFs system. The reversible flow curve of the two-phase STFs system is shown in Fig. 10. The solid line represents the shear rate from low to high (forward test), whereas the dashed line represents the shear rate from high to low (reverse test), which was evaluated to determine whether the two-phase STFs system possesses reversibility. Both curves exhibited shear thinning and thickening in the low shear rate region, but did not completely overlap in the high shear rate region. The above phenomena indicate that the two-phase STFs system has good reversibility, and the nanoparticle cluster structure damaged caused by shear efficiently reorganizes and reconstructs the network structure.[29] Additionally, the peak viscosities and overall curves of the reverse tests were lower than those of the

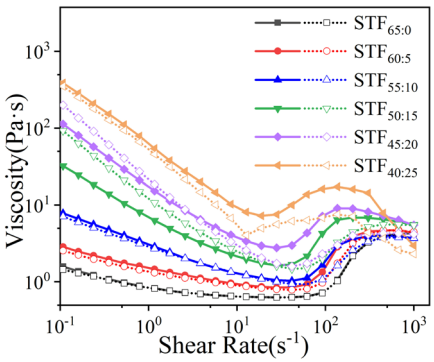

Fig. 10 Reversible flow curves of the two-phase STFs system at 25 °C.

forward tests because the network microstructure damaged by the forward shear was not completed recovered during the reverse shear process.

3.3 Relationship between the rheological and electrical properties of the two-phase STF system

The relationship between the steady-state rheological and electrical properties of $STF_{45:20}$ and PEG200 is shown in Fig. 11a and b. Comparing the shear rate-viscosity and resistance curves of PEG200 and the two-phase STFs system, the viscosity and resistance of PEG200 do not change with increasing shear rate, but the resistance and viscosity of $STF_{45:20}$ decreased and increased, respectively, exhibiting a negative correlation. During the shear thinning stage of the STFs system, the resistance remained stable at 936.77 kΩ. When the system exhibited shear thickening, the resistance rapidly decreased to the lowest value of 795.16 kΩ with the rapid increase in the viscosity. Thus, the variation in the viscosity and resistance occurred simultaneously during the shear process. Because when the STFs system is in the shear thinning stage, there is less contact between the dispersed phase particles owing to the repulsive forces between the molecules, and therefore electron transfer in the polymer solution is difficult, as shown in Fig. 9(e1 and e2). However, when the system is in the shear thickening stage, the rapidly formed SiO_2 and SiO_2@Ag mixed particle hydroclusters have surface contact and Ag on the core–shell microsphere surface more efficiently performs electron transfer, thus reducing the resistance of the system, as shown in Fig. 9(e3).

The relationship between the resistance of the two-phase STFs system and the shear rate for different ratios of the dispersed phases is shown in Fig. 11c. Although no SiO_2@Ag core–shell microspheres were added to the $STF_{65:0}$ system, the variation in resistance also exhibited a similar trend. Because SiO_2 is a semiconductor, the SiO_2 clusters formed in the shear thickening process will also transfer electrons owing to contact with each other, but the resistance transfer efficiency is relatively low. Therefore, the resistance of the STFs system is considerable. For the $STF_{60:5}$ system, the stable resistance without shear thickening was 1423.15 kΩ, and the minimum resistance was 1030.39 kΩ, whereas the stable resistance for the $STF_{45:20}$ system was 936.77 kΩ and the minimum resistance was 795.16 kΩ. Thus, with increasing conducting SiO_2@Ag core–shell microspheres, the stable resistance of the STFs system during shear thinning process decreased and the lowest resistance in the shear thickening process decreased significantly. Additionally, a positive correlation was observed between the resistance change rate and thickening rate of the two-phase STFs system, and the thickening rate of the $STF_{40:25}$ system was 239% with a resistance change rate of 17.17%. Furthermore, the thickening rate of the $STF_{60:5}$ system was 565% with a resistance change rate of 27.6%. Thus, the higher the shear thickening, the more pronounced the change in resistance. This phenomenon further confirms that the synchronous variation in the resistance and viscosity of the two-phase STFs system in Fig. 11a is caused by the change of the microscopic agglomeration of the dispersed phase during the shear thickening process. However, the resistance of the STF system did not continue to decrease with the further increase in the proportion of the SiO_2@Ag core–shell microspheres. In particular, the stability and minimum resistance of $STF_{40:25}$ were higher than those of $STF_{45:20}$. Based on the analysis of the shear thickening

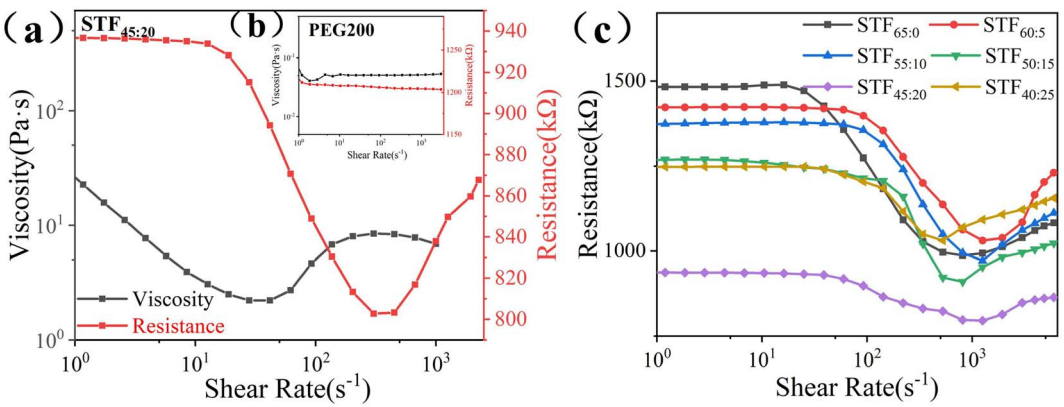

Fig. 11 (a) The relationship between the rheological and electrical properties of the two-phase STFs system; inset (b) diagram of the relationship between the rheological and electrical properties of PEG200; (c) the relationship between the resistance change with shear rate of the two-phase STFs systems prepared with varying dispersed phase ratios at 25 °C.

mechanism of the two-phase STFs system in Section 3.2.1, the surface of the core–shell microspheres possesses limited Si–OH groups, and hydrocluster formation during the shear thickening process depends more on the contact friction and intermolecular force between SiO_2 and the core–shell microspheres. In this case, the excessive addition of core–shell microspheres hinders the ability of SiO_2@Ag to participate in SiO_2 hydrocluster formation during shear thickening completely, and thus the core–shell microspheres are partially dispersed in the polymer solution. Compared with $STF_{45:20}$, the SiO_2 content in $STF_{40:25}$ was relatively lower, and the number of core–shell microspheres that could participate in agglomeration was also lower, and thus it was more difficult to form a conductive pathway, leading to an increase in the resistance of the two-phase STFs system.

Based on the above studies on the rheological properties and resistance changes of the SiO_2/SiO_2@Ag two-phase STFs system, the two-phase conductive $STF_{45:20}$ system with a specific ratio of SiO_2 and SiO_2@Ag in the dispersed phase exhibited a good shear thickening effect. Moreover, a remarkable electrical phenomenon was observed that the resistance of the system decreases rapidly with shear thickening. Therefore, it is possible to fabricate flexible composites with both anti-stab performance and sensing function.

4 Conclusions

In this study, the relationship between the process parameters of conducting SiO_2@Ag core–shell microspheres and their surface morphology and electrical properties was investigated, and the influence of the ratio of the dispersed phases on the rheological properties and resistance of the SiO_2/SiO_2@Ag two-phase STFs system was evaluated, the main conclusions are as follows:

(1) By investigating the effect of the NaOH and $C_6H_{12}O_6$ concentrations on the electroless silver plating process, it is demonstrated that the alkaline environment and reducing agent concentration influenced the morphology of the SiO_2@Ag core–shell microspheres. The optimal process parameters of the NaOH and $C_6H_{12}O_6$ concentrations were 0.07 and 0.09 mol L^{-1}, respectively. Under these conditions, the elemental Ag on the SiO_2@Ag core–shell microsphere surface was uniform and compact and exhibited the lowest resistivity (0.56 Ω cm).

(2) SiO_2/SiO_2@Ag two-phase STFs exhibited a significant shear thickening effect and good reversibility. With increasing SiO_2@Ag core–shell microsphere concentration, the critical shear rate of the system decreased, and the initial and maximum viscosities increased.

(3) When the shear thickening phenomenon occurs in the two-phase STFs system, the resistance decreases simultaneously with the viscosity increase. Moreover, the resistance was the lowest when the shear thickening effect was the most significant. The two-phase $STF_{45:20}$ system exhibited a thickening rate of 325% and minimum resistance of 795.16 kΩ, which was determined to be suitable for fabricating flexible STF-based stab-resistant materials with strain-sensing functions.

(4) During the shear thickening process of the two-phase STFs system, strong surface contact occurs owing to the rapid formation of SiO_2 and SiO_2@Ag hydroclusters, the Ag on the core–shell microsphere surface is more effective for electron transfer, thereby rapidly reducing the resistance of the STFs system. Thus, the resistance and shear thickening behavior simultaneously induce.

The conductive SiO_2@Ag core–shell microspheres investigated in this study provide a novel strategy for the synthesis of multiphase conductive STFs. Moreover, this study provides a new opportunity to explore STFs-based flexible stab-resistant materials for application in the field of strain sensing body armor.

Author contributions

Caiting He: Investigation, data curation, visualization, writing-original draft. Qiushi Wang: conceptualization, methodology, funding acquisition. Xiaoya Jia: data curation, visualization. Jie Liu: validation, visualization, Runjun Sun: methodology, resources. Meiyu Chen: conceptualization, writing-review&editing supervision.

Conflicts of interest

The authors declare that they have no known competing financial interests or personal relationships that could have appeared to influence the work reported in this paper.

Acknowledgements

This work was supported by the Scientific Research Program Funded by the Shaanxi Provincial Education Department (Program No. 21JY015), the Doctoral Scientific Research Foundation of Xi'an Polytechnic University (Program No. BS2020004) and the Science and Technology Guidance Foundation of China National Textile and Apparel Council (Program No. 2020041).

References

1 F. J. Galindo-Rosales, S. Martínez-Aranda and L. Campo-Deaño, CorkSTFμfluidics – a novel concept for the development of eco-friendly light-weight energy absorbing composites, *Mater. Des.*, 2015, **82**, 326–334.
2 A. Majumdar, B. S. Butola and A. Srivastava, Optimal designing of soft body armour materials using shear thickening fluid, *Mater. Des.*, 2013, **46**, 191–198.
3 S. Gürgen, W. Li and M. C. Kuşhan, The rheology of shear thickening fluids with various ceramic particle additives, *Mater. Des.*, 2016, **104**, 312–319.
4 L. L. Sun, D. S. Xiong and C. Y. Xu, Application of shear thickening fluid in ultra high molecular weight polyethylene fabric, *J. Appl. Polym. Sci.*, 2013, **129**(4), 1922–1928.
5 B. J. Maranzano and N. J. Wagner, The effects of particle size on reversible shear thickening of concentrated colloidal dispersions, *J. Chem. Phys.*, 2001, **114**(23), 10514–10527.

6 H. Zhou, L. Yan, W. Jiang, S. Xuan and X. Gong, Shear thickening fluid–based energy-free damper: Design and dynamic characteristics, *J. Intell. Mater. Syst. Struct.*, 2014, **27**(2), 208–220.

7 Q. Chen, M. Liu, S. H. Xuan, W. Q. Jiang, S. S. Cao and X. L. Gong, Shear dependent electrical property of conductive shear thickening fluid, *Mater. Des.*, 2017, **121**, 92–100.

8 B. Liu, C. Du and Y. Fu, The preparation process of shear thickening materials and the application in hydraulic shock absorber, *IOP Conf. Ser.: Earth Environ. Sci.*, 2021, **639**(1), 012040.

9 Y. S. Lee, E. D. Wetzel and N. J. Wagner, The Ballistic Impact Characteristics of Kevlar Woven Fabrics Impregnated with a Colloidal Shear Thickening Fluid, *J. Mater. Sci.*, 2003, **38**(13), 2825–2833.

10 D. P. Kalman, R. L. Merrill, N. J. Wagner and E. D. Wetzel, Effect of particle hardness on the penetration behavior of fabrics intercalated with dry particles and concentrated particle-fluid suspensions, *ACS Appl. Mater. Interfaces*, 2009, **1**(11), 2602–2612.

11 G. Grover, S. K. Verma, A. Thakur, I. Biswas and D. Bhatacharjee, The effect of particle size and concentration on the ballistic resistance of different shear thickening fluids, *Mater. Today: Proc.*, 2020, **28**, 1472–1476.

12 X. Feng, S. Li, Y. Wang, Y. Wang and J. Liu, Effects of different silica particles on quasi-static stab resistant properties of fabrics impregnated with shear thickening fluids, *Mater. Des.*, 2014, **64**, 456–461.

13 S. Gurgen and M. C. Kushan, The stab resistance of fabrics impregnated with shear thickening fluids including various particle size of additives, *Composites, Part A*, 2017, **94**, 50–60.

14 M. Hasanzadeh and V. Mottaghitalab, Tuning of the rheological properties of concentrated silica suspensions using carbon nanotubes, *Rheol. Acta*, 2016, **55**(9), 759–766.

15 M. Hasanzadeh, V. Mottaghitalab, H. Babaei and M. Rezaei, The influence of carbon nanotubes on quasi-static puncture resistance and yarn pull-out behavior of shear-thickening fluids (STFs) impregnated woven fabrics, *Composites, Part A*, 2016, **88**, 263–271.

16 D. Li, R. Wang, X. Liu, S. Fang and Y. Sun, Shear-thickening fluid using oxygen-plasma-modified multi-walled carbon nanotubes to improve the quasi-static stab resistance of Kevlar fabrics, *Polymers*, 2018, **10**(12), 1356.

17 J. S. Zhang, Y. Wang, H. X. Deng, J. Y. Zhou, S. Liu, J. P. Wu, *et al.*, A high anti-impact STF/Ecoflex composite structure with a sensing capacity for wearable design, *Composites, Part B*, 2022, **233**, 109656.

18 M. Zarei and J. Aalaie, Application of shear thickening fluids in material development, *J. Mater. Res. Technol.*, 2020, **9**(5), 10411–10433.

19 J. Zhang, Y. Wang, H. Deng, J. Zhou, S. Liu, J. Wu, *et al.*, A high anti-impact STF/Ecoflex composite structure with a sensing capacity for wearable design, *Composites, Part B*, 2022, **233**, 109656.

20 S. Wang, S. Xuan, M. Liu, L. Bai, S. Zhang, M. Sang, *et al.*, Smart wearable Kevlar-based safeguarding electronic textile with excellent sensing performance, *Soft Matter*, 2017, **13**(13), 2483–2491.

21 M. Liu, S. S. Zhang, S. Liu, S. S. Cao, S. Wang, L. F. Bai, *et al.*, CNT/STF/Kevlar-based wearable electronic textile with excellent anti-impact and sensing performance, *Composites, Part A*, 2019, **126**, 105612.

22 J. Zhou, J. Zhang, M. Sang, S. Liu, F. Yuan, S. Wang, *et al.*, Advanced functional Kevlar composite with excellent mechanical properties for thermal management and intelligent safeguarding, *Chem. Eng. J.*, 2022, **428**, 131878.

23 S. Zhang, S. Wang, Y. Wang, X. Fan, L. Ding, S. Xuan, *et al.*, Conductive shear thickening gel/polyurethane sponge: A flexible human motion detection sensor with excellent safeguarding performance, *Composites, Part A*, 2018, **112**, 197–206.

24 C. Zhao, Y. Wang, S. Cao, S. Xuan, W. Jiang and X. Gong, Conductive shear thickening gel/Kevlar wearable fabrics: A flexible body armor with mechano-electric coupling ballistic performance, *Compos. Sci. Technol.*, 2019, **182**, 107782.

25 T. Fan, Z. Sun, Y. Y. Zhang, Y. Q. Li, Z. K. Chen, P. Huang, *et al.*, Novel Kevlar fabric composite for multifunctional soft body armor, *Composites, Part B*, 2022, **242**, 110106.

26 A. Sakthisabarimoorthi, S. A. M. B. Dhas and M. Jose, Fabrication and nonlinear optical investigations of SiO 2 @Ag core-shell nanoparticles, *Mater. Sci. Semicond. Process.*, 2017, **71**, 69–75.

27 J. C. Flores, V. Torres, M. Popa, D. Crespo and J. M. Calderón-Moreno, Preparation of core–shell nanospheres of silica–silver: SiO2@Ag, *J. Non-Cryst. Solids*, 2008, **354**(52–54), 5435–5439.

28 D. P. Kalman and N. J. Wagner, Microstructure of shear-thickening concentrated suspensions determined by flow-USANS, *Rheol. Acta*, 2009, **48**(8), 897–908.

29 M. Yu, X. Qiao, X. Dong and K. Sun, Shear thickening effect of the suspensions of silica nanoparticles in PEG with different particle size, concentration, and shear, *Colloid Polym. Sci.*, 2018, **296**(7), 1119–1126.